scientific reports

Check for updates

OPEN

Manganese ferrite-graphite oxide-chitosan nanocomposite for efficient dye removal from aqueous and textile wastewater under UV and sunlight irradiation

Nazila Mohammad Hosseini, Shabnam Sheshmani✉ & Ashraf S. Shahvelayati

This study presents the development and characterization of manganese ferrite ($MnFe_2O_4$)-based nanocomposites with graphite oxide (GO) and chitosan (CS) for efficient dye removal from textile wastewater and aqueous solution. Comprehensive characterization was performed using FT-IR, Raman, XRD, BET, SEM, DRS and Zeta potential techniques. XRD analysis confirmed the cubic spinel structure of $MnFe_2O_4$, with characteristic peaks at $2\theta = 32$, 35, 48, 53, 62, and 64°. BET analysis revealed a high specific surface area of 442.57 m^2/g and a pore diameter of 2.36 nm for the $MnFe_2O_4$/GO/CS nanocomposite. SEM imaging showed polyhedral $MnFe_2O_4$ particles (11–33 nm) deposited on a wrinkled graphite oxide matrix. DRS analysis indicated band gap energies of 3.1 eV for $MnFe_2O_4$, 3.0 eV for $MnFe_2O_4$/GO, and 3.5 eV for $MnFe_2O_4$/GO/CS. Zeta potential measurements showed a positive surface charge (+ 36.8 mV) for $MnFe_2O_4$/GO/CS. The $MnFe_2O_4$/GO/CS nanocomposite exhibited exceptional photocatalytic performance under UV light irradiation. It achieved 99.9 and 99.5% removal of Reactive Red 198 dye and Brilliant Blue FCF 133, respectively. The photocatalytic process followed pseudo-second-order kinetics ($R^2 = 0.99$). In real textile wastewater treatment, the nanocomposite reduced BOD from 889 to 0.86 mg/L and COD from 1227 to 74 mg/L, with 96% dye removal. Also, $MnFe_2O_4$/GO/CS showed excellent performance under sunlight irradiation and maintained high removal efficiencies over multiple cycles, demonstrating good reusability. This study highlights the potential of the $MnFe_2O_4$-based nanocomposites as versatile and sustainable solutions for remediating dye-contaminated water.

Keywords Manganese ferrite, Graphite oxide, Chitosan, Dye removal, Photodegradation

Textile industries significantly contribute to water pollution through the discharge of dye-containing effluents. Annually, this sector releases millions of cubic meters of dye-contaminated wastewater. These persistent dyes pose sever threats to aquatic ecosystems and human health, accumulating in the food chain and exhibiting carcinogenic and mutagenic effects. Conventional wastewater treatment methods often prove inadequate in effectively removing these dyes. Processes like coagulation, flocculation, and biological treatment demonstrate limited efficiency against the complex and recalcitrant nature of many textile dyes. Moreover, these traditional methods can be costly, energy-intensive, and may generate secondary pollutants requiring further treatment. This environmental challenge necessitates the development of more effective, economical, and sustainable treatment technologies for textile wastewater[1,2].

Development of advanced materials with enhanced adsorption capacity, reusability, and environmental compatibility is a critical need to address this challenge. These novel materials, which may include functionalized nanomaterials, composite adsorbents, or membrane-based systems, offer the potential for more effective and sustainable dye removal. By exhibiting high adsorption capacity, the adsorbents can efficiently capture and concentrate the dyes from the effluent. Furthermore, their reusability and environmental compatibility can contribute to a more circular economy, reducing the overall environmental impact of textile wastewater treatment. Innovative approaches to designing and synthesizing these advanced adsorbent materials are being

Department of Chemistry, College of Basic Sciences, Yadegar-E-Imam Khomeini (RAH) Shahre Rey Branch, Islamic Azad University, Tehran, Iran. ✉email: shabnam_sheshmani@yahoo.com

actively explored. Researchers are investigating strategies such as the incorporation of functional groups to enhance the material's adsorption properties, selectivity, and durability. The synergistic combination of desirable characteristics, such as high surface area, porous structure, and specific surface functionality, can lead develop highly efficient and sustainable dye removal solutions[3–9].

Manganese ferrite is a spinel-type magnetic material with exciting properties, such as chemical stability, high surface area, and catalytic activity[10–15]. Spinel structures can also be modified by doping with non-metal elements, such as boron, nitrogen, or sulfur. Doping with non-metal elements can introduce additional functionalities, such as enhanced catalytic activity, improved optical properties, or increased ion conductivity. Nitrogen-doped spinel catalysts have exhibited enhanced activity and selectivity for various chemical reactions. These modifications of the spinel structure by incorporating graphite oxide (GO), chitosan (CS), or non-metal elements demonstrate the versatility of this crystal structure and its ability to be tailored for a wide range of applications, including energy, environmental, and biomedical technologies[16–19]. The modification of $MnFe_2O_4$ with graphite oxide and chitosan create a more effective nanocomposite for dye removal. GO's high adsorption capacity and large surface area can enhance overall adsorption capabilities and improve charge separation for better photocatalytic performance. Chitosan adds biocompatibility and may improve nanoparticle stability in aqueous solutions. The combination of $MnFe_2O_4$, GO, and CS is expected to produce synergistic effects, tuning the electronic properties of the material for improved photocatalytic applications. This approach seeks to develop a versatile nanocomposite capable of addressing the complex challenges of textile wastewater treatment by removing various dyes under different conditions[19–22].

The study presents the development and characterization of manganese ferrite ($MnFe_2O_4$)-based nanocomposites with graphite oxide and chitosan. This combination integrates the properties of $MnFe_2O_4$, the high adsorption capacity of graphite oxide, and the biocompatibility of chitosan. The research employs various analytical techniques to thoroughly characterize the nanocomposites, including FT-IR, Raman, Zeta potential, XRD, DRS, BET, and SEM. This comprehensive approach provides a detailed understanding of the structural, optical, and surface properties of the materials. The $MnFe_2O_4$/GO/CS nanocomposite demonstrates exceptional photocatalytic performance in removing dyes under both UV and sunlight irradiation. This dual functionality is particularly novel and valuable for practical applications. The study investigates the removal of two different dyes—Reactive Red 198 and Brilliant Blue FCF 133—demonstrating the versatility of the nanocomposite. The research extends beyond synthetic solutions to test the nanocomposite's effectiveness in treating actual textile wastewater, providing insights into its practical applicability. The study highlights the excellent recyclability of the $MnFe_2O_4$/GO/CS nanocomposite, maintaining high removal efficiencies over multiple cycles. This feature contributes to the material's potential as a sustainable solution for water treatment. The study aims to bridge the gap between material design and environmental remediation needs, offering a potential solution to the challenges of textile wastewater treatment.

Materials and methods

Materials

The following materials were used in this study contain ferric chloride ($FeCl_3{\cdot}6H_2O$, 99.9% purity), manganese chloride ($MnCl_2{\cdot}6H_2O$, 99.9% purity), graphite flakes (99.5% purity), potassium chlorate ($KClO_3$, 99.9% purity), nitric acid (HNO_3, 63% purity), sulfuric acid (H_2SO_4, 97% purity), and aqueous ammonia (NH_3(aq), 25% v/v). All chemicals were purchased from Merck and used without further purification. This comprehensive list of high-purity reagents ensures the reliability and reproducibility of the synthesis process for the $MnFe_2O_4$-based nanocomposites. The careful selection of these materials is crucial for achieving the desired properties and performance in dye removal applications.

The reactive dyes used in this study were Reactive Red 198 and Brilliant Blue FCF 133, obtained from D.Z.E Dye Company in the UK. Reactive Red 198 is a single azo reactive dye with a molecular formula of $C_{27}H_{18}ClN_7Na_4O_{16}S_5$, a molecular weight of 984.21 g/mol, and a CAS registry number of 145017-98-7. Brilliant Blue FCF 133 is a non-azo dye with a molecular formula of $C_{37}H_{34}N_2Na_2O_9S_3$, a molecular weight of 792.85 g/mol, and a CAS registry number of 3844-45-9.

Methods

A comprehensive set of analytical techniques was employed to thoroughly characterize the structure, properties, and performance of the nanomaterials. Fourier transform infrared (FT-IR) spectroscopy was conducted on a Thermo AVATAR spectrometer over the wavenumber range of 400–4000 cm^{-1} to identify the characteristic vibration modes of the nanocomposites. Raman spectroscopy using a Takram P50C0R10 system confirmed the vibration modes and chemical structure. Powder X-ray diffraction (XRD) patterns were obtained on a PHILIPS PW1730 diffractometer using Cu K_α radiation, covering the 2θ range from 10 to 80° with a step size of 0.05° per second. Zeta potential analysis was performed on a Horiba Zeta-Dls Zetasizer to characterize the surface charge properties of the nanocomposites. The optical properties of the nanomaterials across the ultraviolet, visible, and near-infrared regions of the electromagnetic spectrum were investigated using Diffuse Reflectance Spectroscopy (DRS) with the S-4100 SCINCO instrument. Brunauer–Emmett–Teller (BET) analysis conducted on a BELSORP Mini II provided information on the surface area and average pore diameter of the $MnFe_2O_4$/GO/CS nanocomposite. BET surface area analysis was performed using a BELSORP Mini II analyzer. Samples were degassed at 150 °C for one hour under vacuum before analysis. Nitrogen adsorption–desorption isotherms were collected at 77 K. The surface area was calculated in the relative pressure range. Morphological characterization and particle size distribution were obtained using scanning electron microscopy (SEM) on a TESCAN MIRA III field emission gun microscope. The dye concentration was measured using UV-Vis spectroscopy with a Cary 60 UV-Vis spectrophotometer from Agilent Technologies (USA). The dye degradation experiments were conducted under the illumination of a 400W mercury vapor lamp, which emits a broad spectrum of wavelengths, including

ultraviolet (UV) radiation. Additionally, the samples were exposed to sunlight in the laboratory, utilizing natural sunlight as a source of light irradiation. This comprehensive array of spectroscopic, diffraction, and microscopic techniques provided a thorough characterization of the structure, properties, and performance of the nanomaterials.

Synthesis of graphite oxide (GO)

Graphite oxide was prepared using a modified Staudenmaier method. A mixture of nitric acid (10 mL) and sulfuric acid (20 mL) was cooled in an ice bath to 0 °C. Graphite powder (1 g) was then carefully added to this acidic mixture. Potassium chlorate (11 g) was gradually introduced over one hour, with careful attention to maintaining a low reaction temperature. The resulting mixture was stirred at room temperature for four days. The black paste-like product was purified by washing with deionized water until reaching a neutral pH. Finally, the graphite oxide residue was dried in an oven at 60 °C. This procedure ensures the efficient oxidation of graphite while minimizing potential hazards associated with the exothermic reaction. The extended stirring period and thorough washing process contribute to production high-quality graphite oxide, which is crucial for the subsequent synthesis of the $MnFe_2O_4$/GO and $MnFe_2O_4$/GO/CS nanocomposites.

Synthesis of $MnFe_2O_4$ nanoparticles

$FeCl_3{\cdot}6H_2O$ (2 mmol) was dissolved in deionized water (15 mL). Then, in a separate beaker, $MnCl_2{\cdot}6H_2O$ (1 mmol) was added to deionized water (15 mL). The contents of these two beakers were then mixed under continuous stirring for 30 min. Then, ammonium hydroxide (25% v/v) solution was added dropwise to the mixture until the pH reached 12. The reaction mixture was transferred into a Teflon-lined autoclave. The autoclave was heated to 180 °C and held at that temperature for 13 h. Upon completion of the reaction, the autoclave was allowed to cool down to room temperature. The resulting precipitates were filtered and washed several times with water and ethanol until the pH reached 7. Finally, the mixed metal oxide product was dried in an oven at 60 °C.

Synthesis of $MnFe_2O_4$/GO nanocomposite

An aqueous solution containing graphite oxide (0.5 g) in deionized water (40 mL) was prepared using an ultrasonic bath for 1 h. Separately, solutions of $FeCl_3{\cdot}6H_2O$ (2 mmol) in deionized water (15 mL) and $MnCl_2{\cdot}6H_2O$ (1 mmol) in deionized water (15 mL) were prepared. The metal chloride solutions were gradually added to the graphite oxide solution under continuous stirring. Subsequently, ammonium hydroxide (25% v/v) solution was added dropwise to the mixture until the pH reached 12. After 30 min of further stirring, the reaction mixture was transferred into a Teflon-lined autoclave and heated in an oven at 180 °C for 13 h. Once the reaction was complete, the autoclave was allowed to cool down to room temperature. The resulting precipitates were filtered and washed with water and ethanol until the pH reached 7. Finally, the prepared $MnFe_2O_4$/GO nanocomposite was dried at 60 °C.

Synthesis of chitosan-coated $MnFe_2O_4$/GO nanocomposite

Initially, chitosan (1 g) was dissolved in acetic acid (1% v/v, 20–30 mL) to form a chitosan solution. Then, $MnFe_2O_4$/GO nanocomposites (0.5 g) were dispersed in deionized water (20 mL). The $MnFe_2O_4$/GO dispersion was added to the chitosan solution, and the mixture was sonicated for 1 h. Afterward, the chitosan solution was slowly added to the $MnFe_2O_4$/GO dispersion and stirred for about 3 h. Finally, the resulting chitosan-coated $MnFe_2O_4$/GO nanocomposite was filtered and dried at 50 °C.

Evaluation of dye removal

Manganese ferrite and their nanocomposites with graphite oxide and chitosan were evaluated for the removal of Reactive Red 198 and Brilliant Blue FCF 133 dyes from aqueous solutions. Batch adsorption experiments were conducted under both UV and sunlight irradiation to assess the influence of light exposure on the dye removal efficiency. The experiments were conducted using a dye solution with a concentration of 20 mg/L and a volume of 25 mL at 25 °C. For effective dye removal, 0.05 g of the photocatalysts were added to the solution and stirred at 150 rpm for 30 min across various pH levels. The mixture was then magnetically separated, and the remaining dye concentration was measured. Dye removal experiments involved varying several parameters. The initial pH was adjusted from 1 to 8, while the initial dye concentration ranged from 10 to 60 mg/L. The photocatalyst dosage was varied between 0.01 to 0.08 g, and the UV irradiation duration was tested from 15 to 120 min. Additional degradation studies were performed under natural sunlight to assess the photocatalyst composites' effectiveness in real-world conditions. These experiments involved exposing the dye solutions to direct sunlight for three days. Also, Control experiments were also conducted by irradiating dye solutions without any photocatalyst under identical conditions. No dye degradation was observed in these control experiments, confirming the necessity of the photocatalyst nanocomposites for the degradation process. The reusability was also investigated through multiple photodegradation cycles. Furthermore, the photodegradation was tested for the treatment of actual textile wastewater samples to evaluate their performance in removing complex dye mixtures. The ability to utilize both UV and sunlight for enhanced dye removal, as well as the reusability and performance in actual wastewater samples, highlights the potential of these nanomaterials for practical water treatment applications.

Results and discussion

Comprehensive structural, optical, microscopic, and surface studies demonstrated the successful incorporation of the $MnFe_2O_4$ nanoparticles, the integration of the graphite oxide sheets, and the coating of the chitosan biopolymer. These comprehensive characterization results provide valuable insights into the structural,

compositional, and functional attributes of the developed nanomaterials, which can guide further optimization and applications in water treatment fields.

Structural studies

The FT-IR spectroscopy provides valuable insights into the molecular structure and bonding characteristics of $MnFe_2O_4$-based nanocomposites. Figures 1a,b show the FT-IR spectra of the $MnFe_2O_4$/GO and $MnFe_2O_4$/GO/CS, respectively. In Fig. 1a, the peaks in the region of 400 to 500 cm^{-1} are attributed to the Fe–O and Mn–O bonds, which are characteristic of the spinel structure of $MnFe_2O_4$. The peaks in the region of 1000 to 1700 cm^{-1} are assigned to the stretching vibrations of the C–O and C=O bonds of graphite oxide. The peak around 3000 cm^{-1} is attributed to the stretching vibrations of the C–H bonds, while the broadband in the region of 3400 to 3600 cm^{-1} is assigned to the stretching vibrations of the O–H hydroxyl groups. In the FT-IR spectrum of the $MnFe_2O_4$/GO/

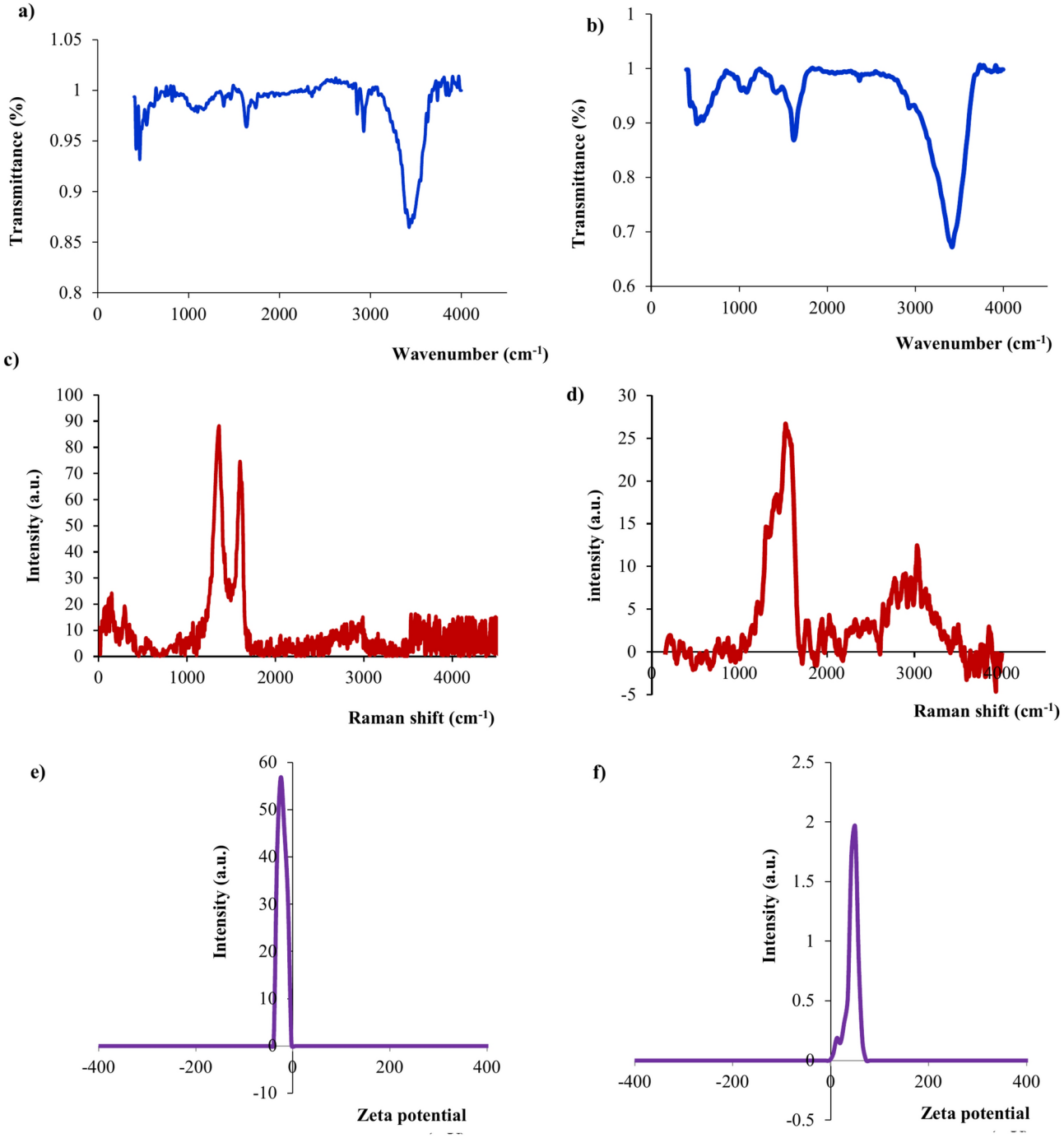

Fig. 1. Structural studies (**a**,**b**) FT-IR spectra of $MnFe_2O_4$/GO and $MnFe_2O_4$/GO/CS, (**c**,**d**) Raman spectra of $MnFe_2O_4$/GO and $MnFe_2O_4$/GO/CS, (**e**,**f**) Zeta potential of $MnFe_2O_4$/GO and $MnFe_2O_4$/GO/CS.

CS nanocomposite (Fig. 1b), the intense stretching vibrations in the region around 3400 cm^{-1} can be attributed to the N–H and O–H bonds present in the structure of chitosan and graphite oxide. Furthermore, the stretching vibration in the range of 500 cm^{-1} is related to the metal-oxygen stretching vibrations, confirming the presence of the $MnFe_2O_4$ spinel structure[19–21].

Figure 1c,d present the Raman spectra of the $MnFe_2O_4$/GO and $MnFe_2O_4$/GO/CS nanocomposites, respectively. Raman spectroscopy provides complementary information to FT-IR analysis about the molecular structure and composition of these nanocomposites. The peak observed in the region of 400 to 500 cm^{-1}, known as the E_g mode, indicates multiple vibrations related to the metal-oxygen bonds, such as Fe–O and Mn–O, characteristic of the $MnFe_2O_4$ spinel structure. The peaks in the range of 1300 cm^{-1} are attributed to the defects and disorders in the graphite network, commonly referred to as the D-band. The peak around 1580 to 1600 cm^{-1} corresponds to the stretching of the sp^2 carbon atoms in the graphite lattice, known as the G-band. For the $MnFe_2O_4$/GO/CS nanocomposite (Fig. 1d), the broad peak in the region of 2880 to 3000 cm^{-1} is attributed to the vibrations related to the chitosan component of the nanocomposite material[20].

Zeta potential is a fundamental physicochemical property that reveals insights into the surface charge and stability of colloidal systems. The zeta potential shows the electrical potential at the interface between the material surface and the surrounding liquid environment. These potential measures the surface charge and can influence various processes, including particle aggregation, dispersion, and surface interactions. The sign and magnitude of the zeta potential can vary depending on factors such as pH, ionic strength, and the composition of the surrounding environment. Zeta potential values can be positive, negative, or near zero. As shown in Fig. 1e,f, the zeta potential analysis reveals distinct surface charge characteristics for the two nanocomposites. The $MnFe_2O_4$/GO nanocomposite exhibits a negative surface charge (−24.7 mV), indicating the presence of negatively charged functional groups or species on the material surface. In contrast, the $MnFe_2O_4$/GO/CS nanocomposite displays a positive zeta potential peak (+36.8 mV). This positive surface charge can be attributed to amine functional groups from the chitosan component. In a slightly acidic environment, these amine groups can become protonated, resulting in the release of positive ions and a net positive surface charge. The positive zeta potential of the $MnFe_2O_4$/GO/CS nanocomposite suggests its potential for applications where interaction with negatively charged species or surfaces is desirable, such as in adsorption processes and targeted drug delivery systems.

XRD is a powerful technique for investigating the crystalline structure and composition of materials, including the $MnFe_2O_4$/GO and $MnFe_2O_4$/GO/CS nanocomposites. Manganese ferrite, $MnFe_2O_4$, is a spinel compound with a cubic face-centered crystal structure, where the iron and manganese cations are located in the octahedral and tetrahedral sites within the lattice. The JCPDS card number for $MnFe_2O_4$ is 75–0034. The critical information from the JCPDS data includes its cubic crystal system with space group Fd3m, lattice parameter of a = 8.49 Å. As shown in Fig. 2, the presence of distinct diffraction peaks at 2θ = 32, 35, 48, 53, 62, and 64° indicates the formation of the cubic spinel structure of $MnFe_2O_4$. The broad peak around 2θ = 10° is evidence of the presence of graphite oxide, a characteristic feature of the graphene oxide component in the nanocomposites[20]. Furthermore, the diffraction peak at 2θ = 20° is attributed to the chitosan component in the $MnFe_2O_4$/GO/CS nanocomposite. These analyses further prove the successful incorporation of $MnFe_2O_4$, graphite oxide, and chitosan within the nanocomposite structures.

Optical studies

The band gap energies of the $MnFe_2O_4$, $MnFe_2O_4$/GO, and $MnFe_2O_4$/GO/CS nanocomposites were investigated using DRS, as shown in (Fig. 3). By analyzing the absorption spectra obtained from the DRS measurements, it is possible to determine the band gap of the composite materials. The absorption peaks observed in the spectra correspond to the onset of electronic transitions within the composites. As shown in Fig. 3a, the band gap of the pure $MnFe_2O_4$ nanoparticles was determined to be around 3.1 eV. This value suggests that $MnFe_2O_4$ is a narrow-band gap semiconductor material. Examining the $MnFe_2O_4$/GO nanocomposite, the band gap value was found to decrease to approximately 3.0 eV, as depicted in (Fig. 3b). This decrease in band gap energy can be attributed to the interactions between the $MnFe_2O_4$ nanoparticles and the graphite oxide component in the composite. Furthermore, the $MnFe_2O_4$/GO/CS nanocomposite exhibited an increased band gap of 3.5 eV, as shown in (Fig. 3c). The addition of the chitosan component to the $MnFe_2O_4$/GO nanocomposite appears to have influenced the electronic transitions and widened the band gap of the resulting material. The variations in band gap values observed for the different nanocomposites suggest that the incorporation of GO and CS can effectively tune the electronic properties of the $MnFe_2O_4$ material. This tunability of the band gap opens up possibilities for tailoring the optical and electronic characteristics of the nanocomposites for various applications, such as optoelectronics, photocatalysis, and energy-related devices[23,24].

Surface studies

Brunauer–Emmett–Teller (BET) analysis is a widely used method for determining the surface area of materials. The BET analysis involves measuring the amount of gases adsorbed such as nitrogen or argon at different relative pressures onto the surface of a solid material. By plotting these parameters, the specific surface area can be calculated using the BET equation. The BET equation assumes that the gas molecule adsorption occurs in a monolayer on the surface, and the specific surface area is determined by extrapolating the adsorption isotherm to a relative pressure of zero. In addition to surface area determination, the Barret-Joyner-Halenda (BJH) method, also known as the BJH technique, is commonly used to analyze the pore size distribution in porous materials. The BJH method utilizes the gas adsorption isotherms obtained from BET experiments, specifically the desorption isotherm branch, to estimate the pore size distribution. The nitrogen adsorption–desorption analysis of the $MnFe_2O_4$/GO/CS nanocomposite was carried out at 77 Kelvin, and the results are shown in (Fig. 4). The specific surface area of the $MnFe_2O_4$/GO/CS nanocomposite was estimated to be 442.57 m^2/g. Additionally, the pore diameter was 2.36 nm (Table 1). This comprehensive BET and BJH analysis provide information into the surface

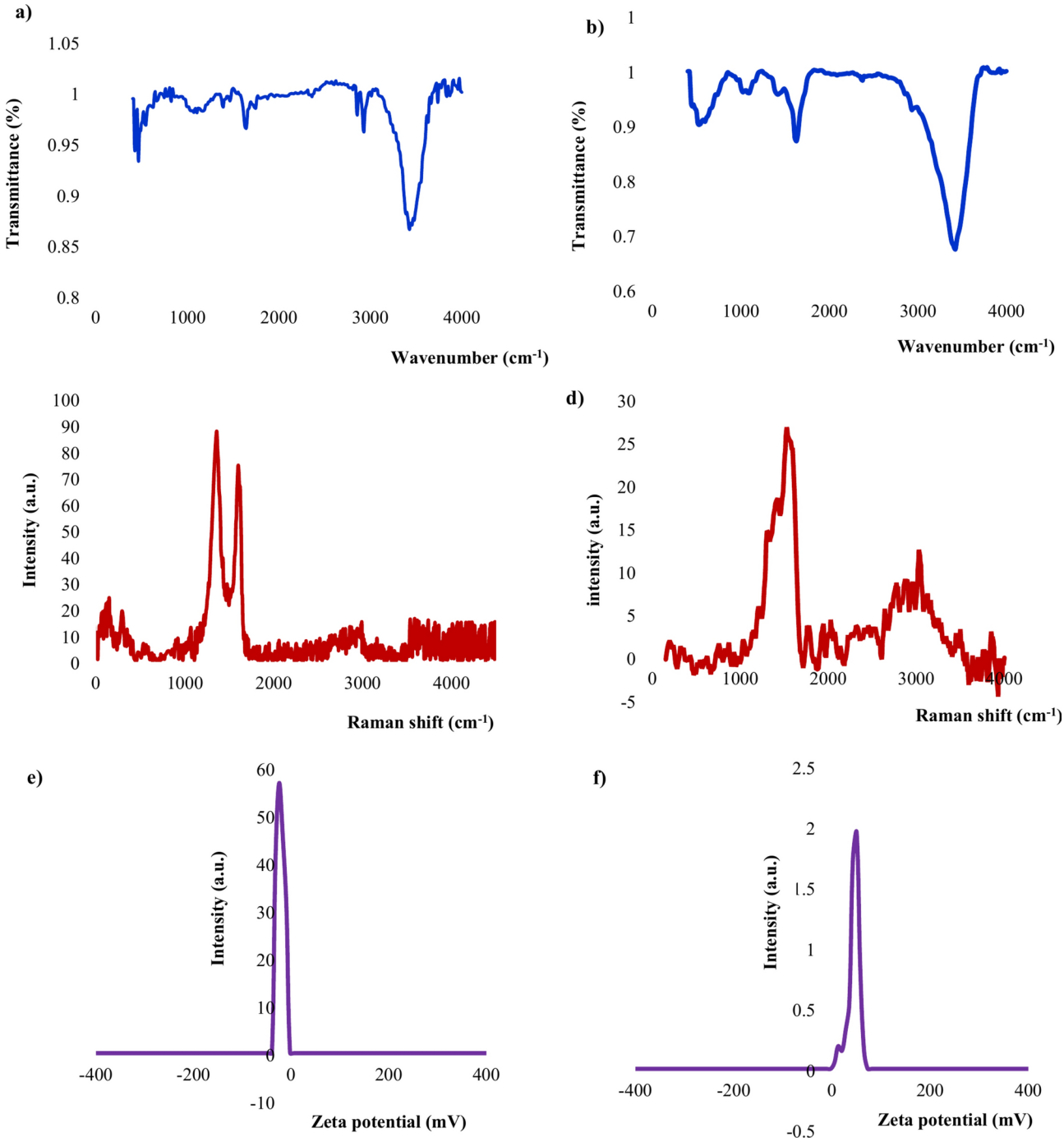

Fig. 2. XRD pattern of $MnFe_2O_4$/GO and $MnFe_2O_4$/GO/CS.

characteristics and porous structure of the $MnFe_2O_4$/GO/CS nanocomposite, which can be important for its potential applications in areas such as photocatalyst and adsorption.

Microscopic studies

The morphology and structural features of the $MnFe_2O_4$/GO nanocomposite were investigated using SEM, as shown in (Fig. 5). The polyhedral particles observed in the SEM images are the $MnFe_2O_4$ nanoparticles with about 11–33 nm in particle size deposited on the graphite oxide matrix. These particles exhibit well-defined shapes and edges, giving them a polyhedral or quasi-polyhedral appearance. Surrounding the $MnFe_2O_4$ particles, the SEM images show a wrinkled graphite oxide layer with a silk-like, thin, and flexible texture. This graphite oxide matrix is spread throughout the composite, acting as a supporting framework for the dispersed $MnFe_2O_4$ nanoparticles. Combining the polyhedral $MnFe_2O_4$ particles and the silk-like graphene oxide layer in the $MnFe_2O_4$/GO nanocomposite suggests an intimate integration of the two components, creating a unique

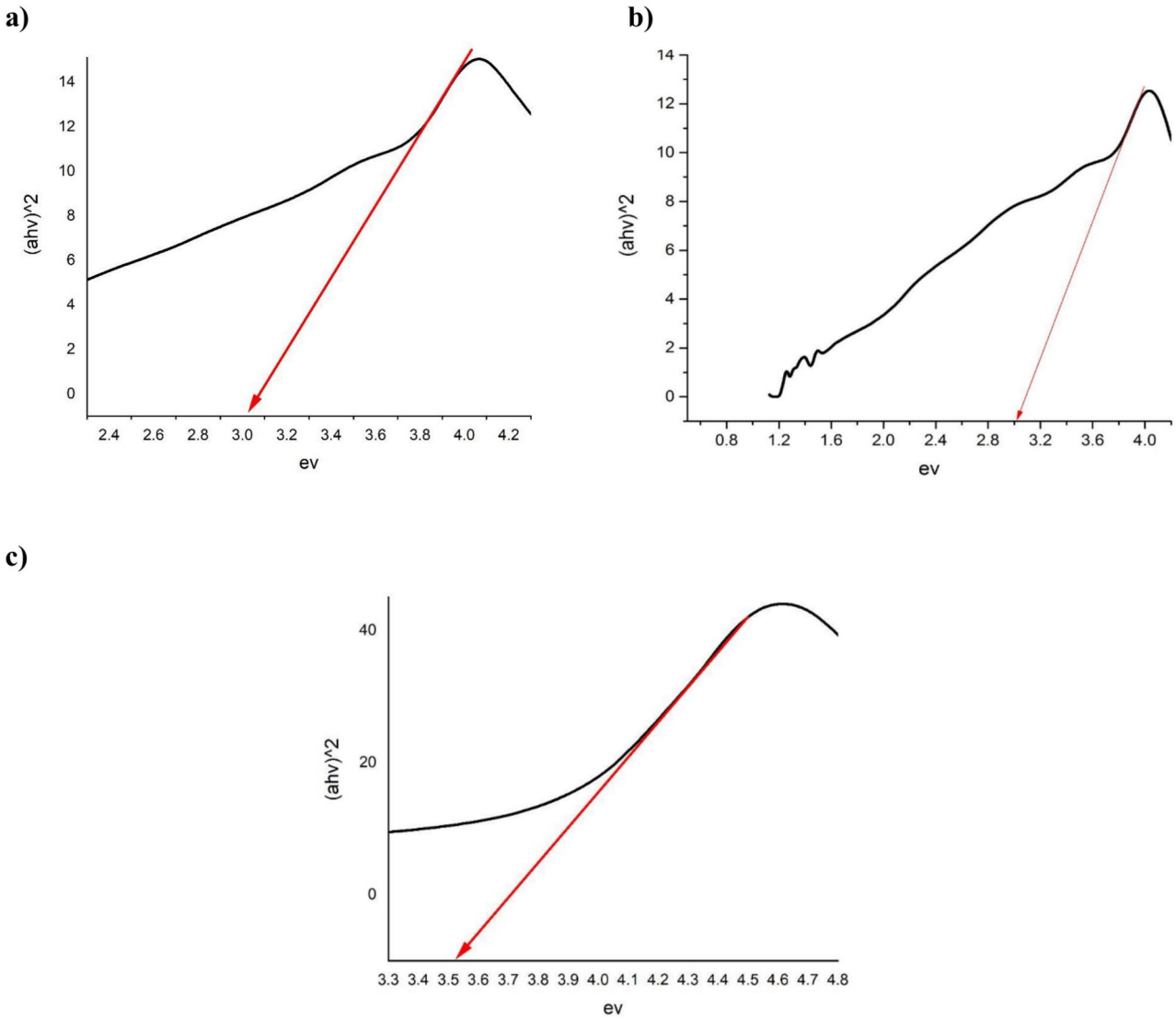

Fig. 3. Band gap values obtained for (**a**) $MnFe_2O_4$, (**b**) $MnFe_2O_4$/GO, and (**c**) $MnFe_2O_4$/GO/CS, respectively.

nanocomposite structure. This synergistic arrangement can potentially enhance the physicochemical properties and performance of the nanocomposite for various applications, such as adsorbent in environmental remediation.

The elemental composition of the $MnFe_2O_4$/GO nanocomposite was thoroughly analyzed using energy-dispersive X-ray spectroscopy (EDS). The EDS spectrum, along with the elemental mapping (Fig. 6), distinctly shows the presence of carbon (51.88 wt.%), oxygen (26.18 wt.%), manganese (0.12 wt.%), and iron (21.82 wt.%), indicating the successful integration of graphite oxide and $MnFe_2O_4$ within the composite. The high carbon content reflects the GO matrix, while the presence of manganese and iron confirms the formation of the $MnFe_2O_4$ phase. The relatively lower manganese content compared to iron suggests a balanced incorporation of these elements, aligning with the stoichiometry of $MnFe_2O_4$. By combining SEM imaging and EDS analysis, detailed insights into the structural morphology and compositional uniformity of the $MnFe_2O_4$/GO nanocomposite are obtained, demonstrating its potential for various applications.

Also, the structural features of the $MnFe_2O_4$/GO/CS nanocomposite were further investigated using SEM, as shown in (Fig. 7). The SEM images confirm the presence of the $MnFe_2O_4$ particles deposited on the graphite oxide matrix. Also, a distinct feature observed in the $MnFe_2O_4$/GO/CS nanocomposite is a chitosan layer on the surface of the graphite oxide. The SEM images clearly show that the chitosan layer continuously coats the $MnFe_2O_4$ nanoparticles and the underlying graphite oxide in a smooth and non-wrinkled manner. This chitosan coating provides a uniform and well-dispersed coverage over the $MnFe_2O_4$/GO components, creating a more homogeneous and integrated nanocomposite structure. The chitosan layer's uniform coating on the $MnFe_2O_4$ particles and graphite oxide matrix suggests a strong interaction and integration between the different components, which could potentially enhance the overall performance and stability of the nanocomposites.

The SEM analysis reveals distinct morphological differences between the $MnFe_2O_4$/GO and $MnFe_2O_4$/GO/CS nanocomposites. The $MnFe_2O_4$/GO composite shows polyhedral $MnFe_2O_4$ nanoparticles (11–33 nm) deposited on a wrinkled, silk-like graphite oxide matrix. In contrast, the $MnFe_2O_4$/GO/CS composite exhibits

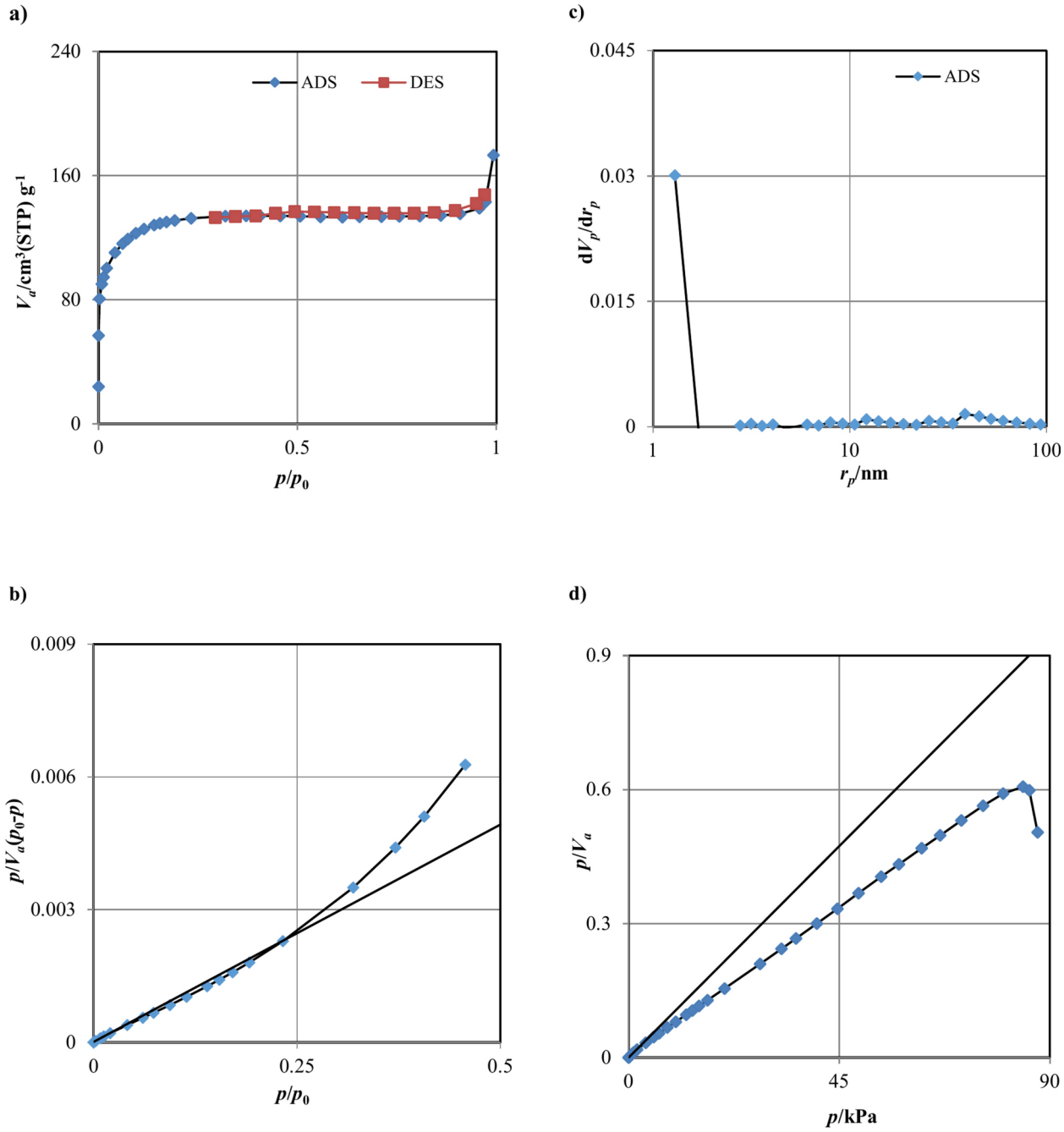

Fig. 4. (**a**) Nitrogen adsorption–desorption isotherm, (**b**) BET analysis, (**c**) BJH curve, and (**d**) Langmuir plot for $MnFe_2O_4$/GO/CS.

a smooth, uniform chitosan layer coating of both the $MnFe_2O_4$ particles and graphite oxide, creating a more homogeneous structure. These morphological differences correlate well with the BET analysis results. The smoother, more integrated surface of the $MnFe_2O_4$/GO/CS likely contributes to its high specific surface area (442.57 m^2/g). The uniform chitosan coating may influence the consistent pore size distribution, with a mean pore diameter of 2.36 nm. The enhanced particle dispersion and integration in the $MnFe_2O_4$/GO/CS composite, as observed in the SEM images, align with the high surface area and uniform pore characteristics revealed by BET analysis. This structure–property relationship explains the superior performance of the $MnFe_2O_4$/GO/CS nanocomposite in dye removal applications, highlighting the synergistic effect of the chitosan coating on the composite's morphology and surface properties[25–27].

Therefore, the images of $MnFe_2O_4$/GO eveal a wrinkled graphite oxide layer with a silk-like, thin, and flexible texture. In contrast, the SEM images of the $MnFe_2O_4$/GO/CS nanocomposite distinctly demonstrate that the chitosan layer forms a continuous, smooth coating over the $MnFe_2O_4$ nanoparticles and the underlying graphite oxide, eliminating the characteristic wrinkled appearance of the graphite oxide layer.

BET plot	
V_m	101.68 $cm^3(STP)\ g^{-1}$
$a_{s,BET}$	442.57 m^2g^{-1}
Total pore volume ($p/p_0 = 0.990$)	0.2617 cm^3g^{-1}
Mean pore diameter	2.3656 nm
Langmuir plot	
V_m	95.068 $cm^3(STP)g^{-1}$
$a_{s,Lang}$	413.78 m^2g^{-1}
B	46.621
t plot	
Plot data	Adsorption branch
a_1	527.65 m^2g^{-1}
V_1	0 cm^3g^{-1}
BJH plot	
Plot data	Adsorption branch
V_p	0.0742 cm^3g^{-1}
$r_{p,peak}$ (Area)	1.29 nm
a_p	30.526 m^2g^{-1}

Table 1. Values of pore size, surface area, and pore volume in BET, Langmuir, t, and BJH plots.

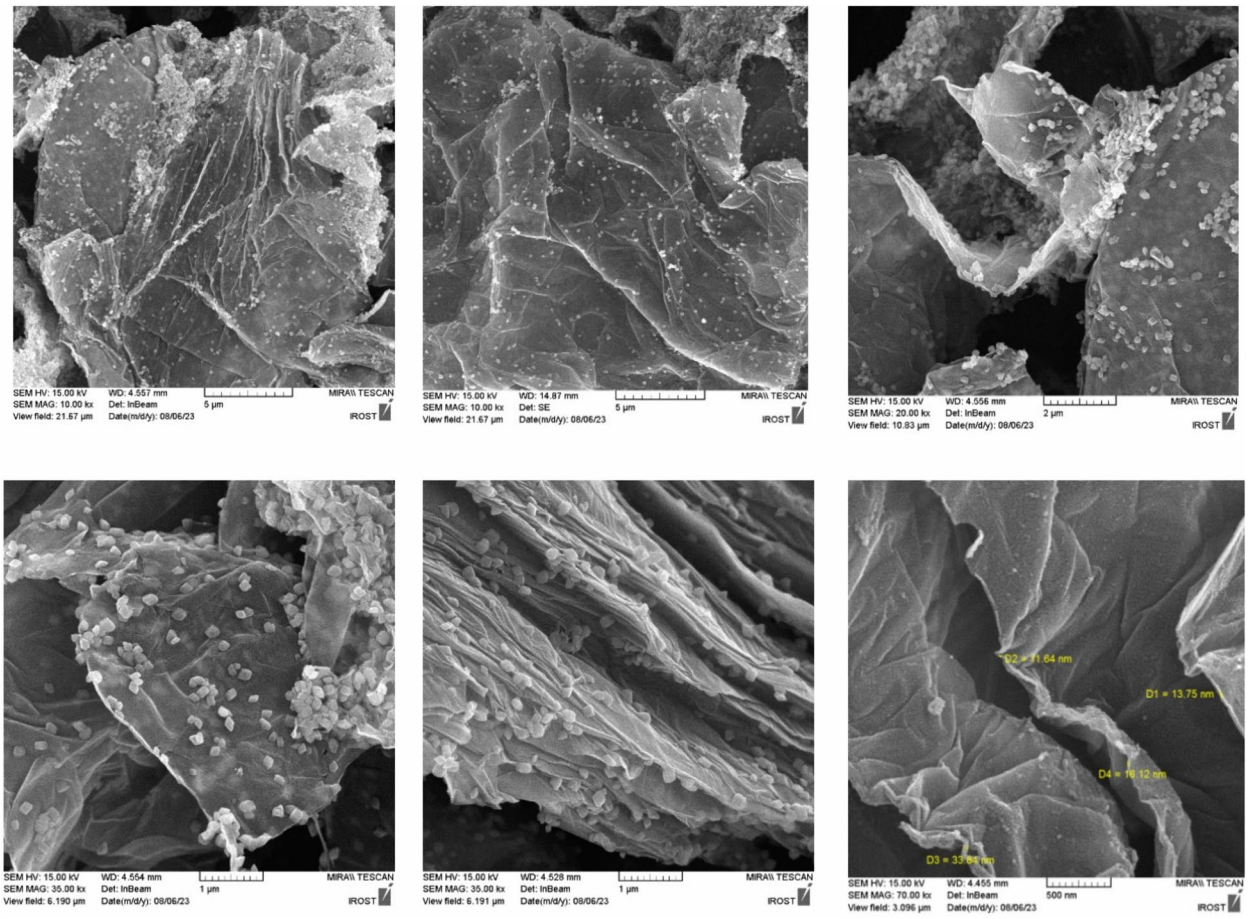

Fig. 5. SEM images of $MnFe_2O_4$/GO nanocomposite.

a)

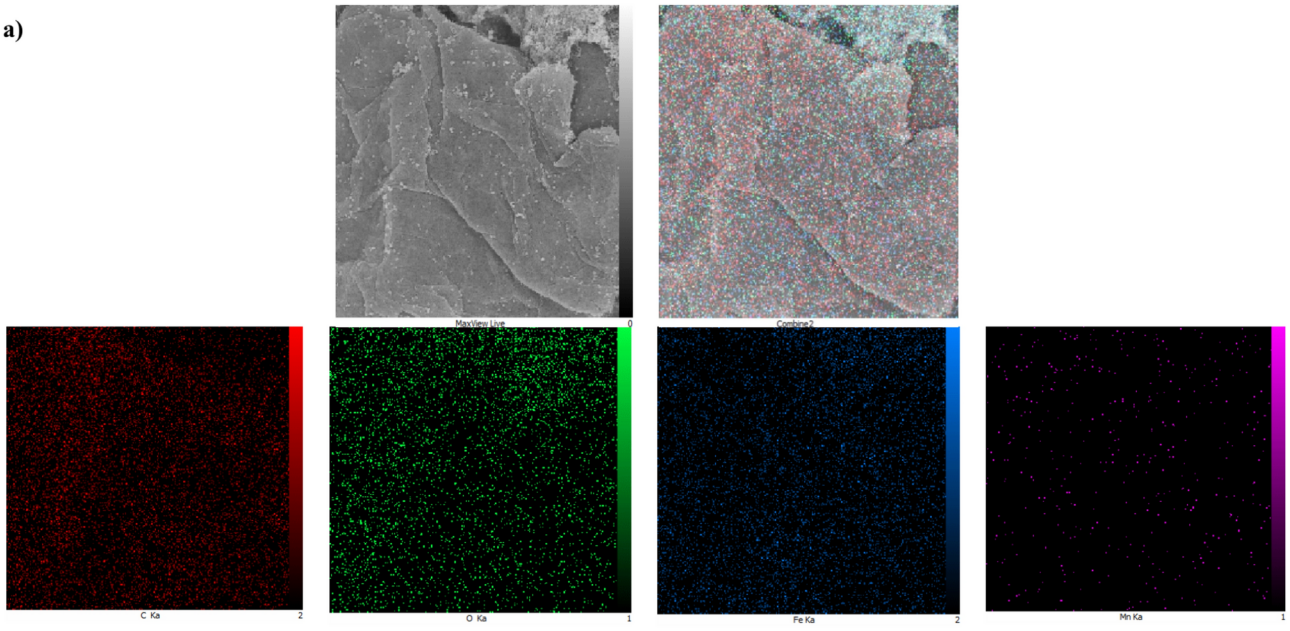

b)

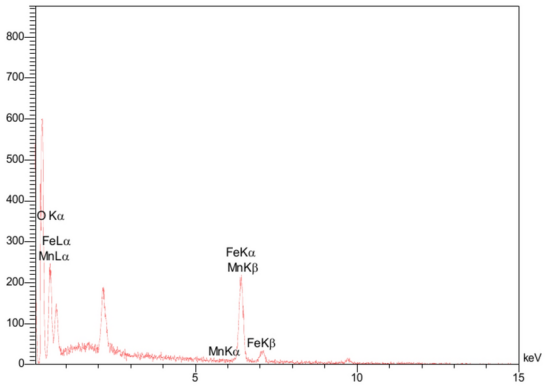

Elt	Line	Int	K	Kr	W%	A%	ZAF	Pk/Bg	LConf	HConf
C	Ka	131.9	0.5173	0.2589	51.88	68.04	0.4990	128.34	50.24	53.53
O	Ka	69.1	0.1350	0.0675	26.18	25.78	0.2579	35.84	25.04	27.33
Mn	Ka	0.7	0.0019	0.0009	0.12	0.03	0.8058	2.10	0.06	0.17
Fe	Ka	101.9	0.3459	0.1731	21.82	6.15	0.7934	18.75	21.03	22.60
			1.0000	0.5005	100.00	100.00				

Fig. 6. (**a**) Mapping images for visualizing element arrangement and (**b**) EDS analysis of $MnFe_2O_4$/GO.

Dye removal performance

The photocatalytic degradation of Reactive Red 198 and Brilliant Blue FCF 133 dyes was investigated using $MnFe_2O_4$ nanoparticles and their composites with graphite oxide and chitosan. The effect of pH on the photocatalytic degradation efficiency was examined. For the $MnFe_2O_4$ nanoparticles and the $MnFe_2O_4$/GO nanocomposite, the maximum dye removal was achieved at pH 1, with 70.2% of the Reactive Red 198 degraded. In acidic conditions, the presence of H^+ ions become more abundant, causing an elevation in the surface charge of the photocatalyst and complexation behavior[28–30]. As the pH increased, the dye removal percentage decreased. In contrast, the $MnFe_2O_4$/GO/CS nanocomposite exhibited a different behavior. At pH 8, the nanocomposite

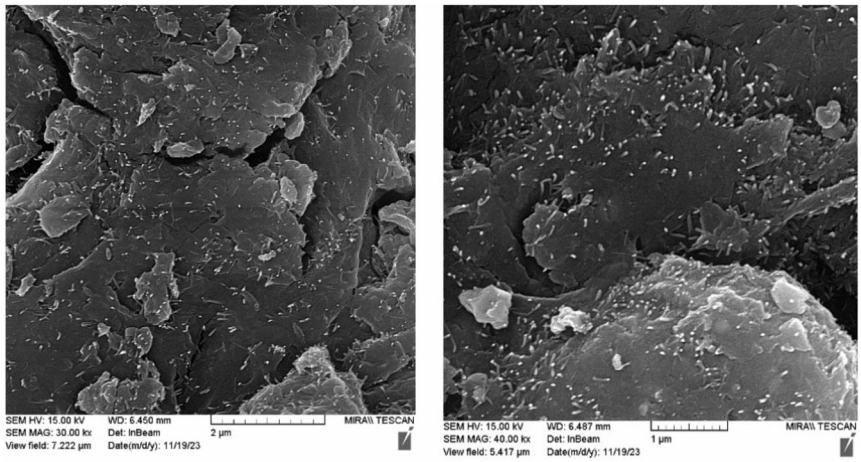

Fig. 7. SEM images of $MnFe_2O_4$/GO/CS nanocomposite.

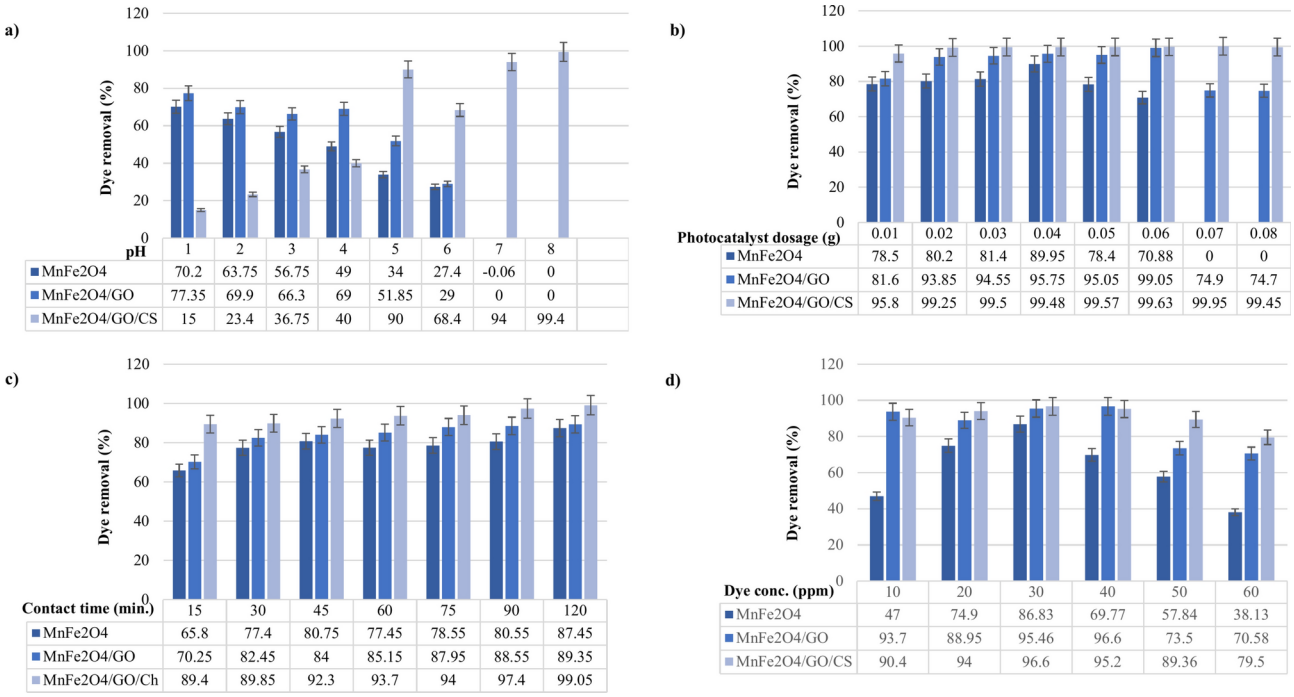

Fig. 8. Effect of (**a**) pH, (**b**) photocatalyst dosage, (**c**) contact time, and (**d**) dye concentration on Reactive Red 198 removal using $MnFe_2O_4$, $MnFe_2O_4$/GO, and $MnFe_2O_4$/GO/CS.

achieved the highest dye removal efficiency, with 99.4% of the Reactive Red 198 being degraded. The improved photocatalytic performance of the $MnFe_2O_4$/GO/CS nanocomposite at higher pH can be attributed to the synergistic effects of the individual components. The graphite oxide provides a large surface area and efficient charge separation, while the chitosan enhances the adsorption property, and swelling behavior. These results demonstrate the potential of $MnFe_2O_4$-based photocatalysts, especially the $MnFe_2O_4$/GO/CS nanocomposite, for effectively removing Reactive Red 198 dyes under different pH conditions (Fig. 8a).

The effect of the photocatalyst dosage on the dye removal efficiency was also investigated. The photocatalyst amount was varied in the range of 0.01 to 0.08 g. For the $MnFe_2O_4$ nanoparticles, the maximum dye removal reached 89.95%. The $MnFe_2O_4$/GO composite exhibited an even higher dye removal efficiency of 95.75% under the optimal photocatalyst dosage. The $MnFe_2O_4$/GO/CS nanocomposite demonstrated the highest overall dye removal performance, achieving 99.48% degradation. Notably, a remarkable dye removal of 99.25% was obtained using only 0.02 g of the $MnFe_2O_4$/GO/CS nanocomposite as the photocatalyst. The enhanced photocatalytic activity of the $MnFe_2O_4$/GO and $MnFe_2O_4$/GO/CS systems can be attributed to the better adsorption capability of the graphite oxide and chitosan components. The synergistic effects of the individual constituents in the composite materials led to superior dye removal performance compared to the standalone $MnFe_2O_4$

nanoparticles. These results highlight the potential of the $MnFe_2O_4$/GO/CS nanocomposite as an efficient and cost-effective photocatalyst for the treatment of dye-containing wastewater, requiring only a tiny amount of the material to achieve remarkably high dye removal rates (Fig. 8b).

The effect of the photocatalytic process duration on the dye removal efficiency was also investigated. After 75 min of the photocatalytic process, the $MnFe_2O_4$ nanoparticles achieved a maximum dye removal of 78.55%. The $MnFe_2O_4$/GO composite exhibited a higher dye removal efficiency of 87.95% under the same conditions. Remarkably, during the same 75 min photocatalytic treatment, the $MnFe_2O_4$/GO/CS nanocomposite demonstrated an exceptionally high dye removal of 94%. The superior photocatalytic performance of the $MnFe_2O_4$/GO/CS nanocomposite can be attributed to the synergistic effects of its components. The combination of these properties in the $MnFe_2O_4$/GO/CS nanocomposite leads to the accelerated degradation of the dye molecules compared to the standalone $MnFe_2O_4$ nanoparticles and the $MnFe_2O_4$/GO nanocomposite. These results highlight the significant potential of the $MnFe_2O_4$/GO/CS nanocomposite as a highly efficient and rapid photocatalyst for treating dye-containing aqueous solution. The nanocomposite's ability to achieve near-complete dye removal within a short 75 min treatment time demonstrates its practical applicability for industrial-scale purification (Fig. 8c).

In this study also the effect of the initial dye concentration on the photocatalytic removal efficiency was investigated. At an initial Reactive Red 198 dye concentration of 20 ppm, the $MnFe_2O_4$ nanoparticles achieved a dye removal percentage of 74.9%. The $MnFe_2O_4$/GO composite exhibited a higher dye removal of 88.95% under the same conditions. When the initial dye concentration was increased to 30 ppm, the dye removal percentage improved for both photocatalysts. The $MnFe_2O_4$ nanoparticles achieved a dye removal of 86.83%, while the $MnFe_2O_4$/GO composite showed an even higher dye removal of 95.46%. The $MnFe_2O_4$/GO/CS nanocomposite demonstrated the best performance at the higher 30 ppm dye concentration, achieving an exceptional dye removal of 96.6%. The improved photocatalytic activity of the composite materials, especially the $MnFe_2O_4$/GO/CS nanocomposite, can be attributed to their increased surface area, enhanced adsorption capacity, and efficient charge separation characteristics. These properties allow the photocatalysts to degrade the dye molecules even at higher initial concentrations. These results highlight the robust and highly efficient nature of the $MnFe_2O_4$/GO/CS nanocomposite, which can maintain exceptional dye removal performance even under challenging conditions with increased dye concentrations. This makes the nanocomposite a promising candidate for practical applications in treating highly concentrated dye-containing wastewater (Fig. 8d).

Also, the photocatalytic removal performance of Brilliant Blue FCF 133 as the target dye was evaluated using $MnFe_2O_4$-based nanocomposites. The results showed that the $MnFe_2O_4$ nanoparticles achieved a maximum dye removal of 88.8%. The $MnFe_2O_4$/GO nanocomposite exhibited a higher dye removal efficiency of 95.5%. Remarkably, the $MnFe_2O_4$/GO/CS nanocomposite demonstrated the best performance, attaining an exceptional dye removal of 99.5%. The superior photocatalytic activity of this nanocomposite, especially the $MnFe_2O_4$/GO/CS, can be attributed to the synergistic effects of their components. These findings further showcase the outstanding photocatalytic capabilities of the $MnFe_2O_4$/GO/CS nanocomposite, which achieved near-complete removal of the Brilliant Blue FCF 133 dye (Fig. 9a–d).

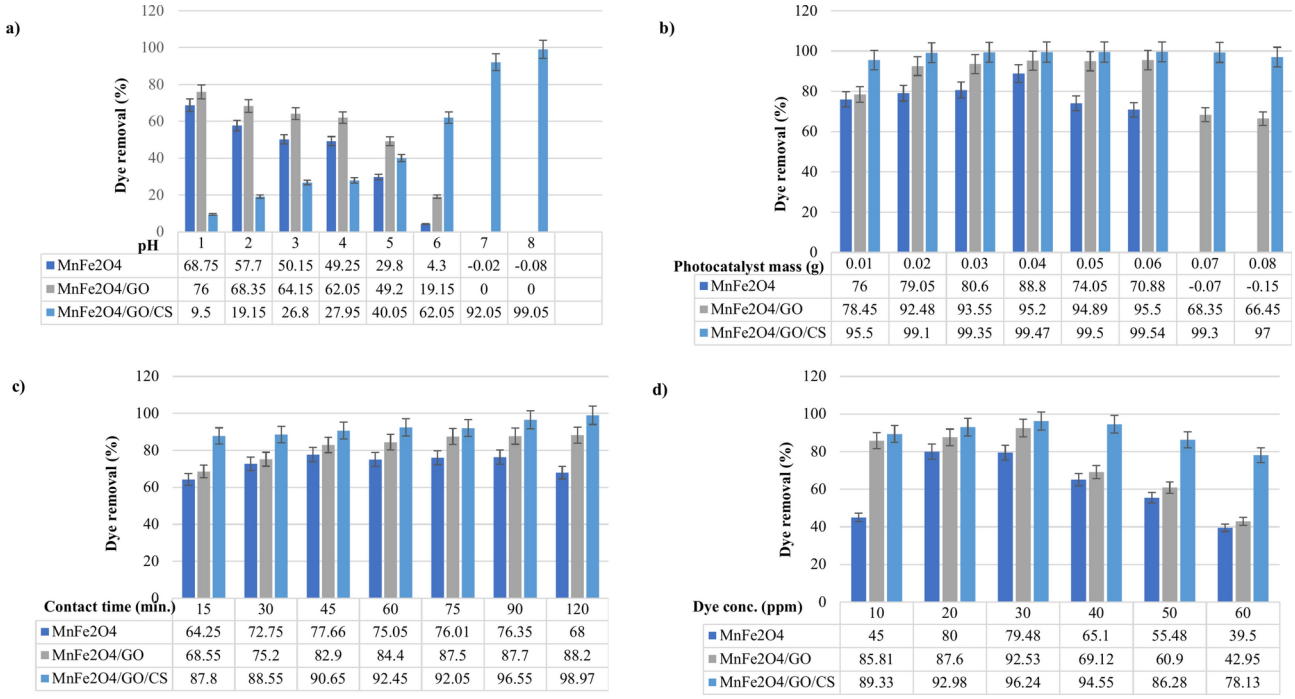

Fig. 9. Effect of (**a**) pH, (**b**) photocatalyst dosage, (**c**) contact time, and (**d**) dye concentration on Brilliant Blue FCF 133 removal using $MnFe_2O_4$, $MnFe_2O_4$/GO, and $MnFe_2O_4$/GO/CS.

The photocatalytic efficiency of $MnFe_2O_4$ nanoparticles and their nanocomposites was investigated under sunlight irradiation. The results revealed that the $MnFe_2O_4$/GO/CS nanocomposite exhibited the best photocatalytic performance compared to the standalone $MnFe_2O_4$ nanoparticles and the $MnFe_2O_4$/GO nanocomposite. These findings highlight the significant potential of the $MnFe_2O_4$/GO/CS nanocomposite as an efficient and versatile photocatalyst for removing various dye pollutants under sunlight illumination (Fig. 10)[31–34].

Kinetic studies

To further understand the kinetics of the photocatalytic dye removal process, both the pseudo-first-order and pseudo-second-order kinetic models were plotted. For removing Reactive Red 198 and Brilliant Blue FCF 133 dyes using the $MnFe_2O_4$/GO/CS nanocomposite, the R^2 value obtained from the pseudo-first-order kinetic model was 0.89 and 0.93, respectively. Similarly, the R^2 value from the pseudo-second-order kinetic equation was 0.99 for both Reactive Red 198 and Brilliant Blue FCF 133 dyes. The higher R^2 values for the pseudo-second-order model, compared to the pseudo-first-order model, suggest that the photocatalytic dye removal kinetics follow the pseudo-second-order kinetics more closely. This indicates that the rate-limiting step in the dye removal process is likely the chemisorption of the dye molecules onto the active sites of the $MnFe_2O_4$/GO/CS nanocomposite. These kinetic analysis results provide valuable insights into the mechanism and rate-controlling steps governing the photocatalytic degradation of the dye pollutants by the $MnFe_2O_4$/GO/CS nanocomposite. This understanding can help optimize the design and operational parameters for effectively implementing the nanocomposite in real-world wastewater treatment applications (Fig. 11).

Reusability of $MnFe_2O_4$/GO/CS in dye removal

An essential aspect in evaluating the photocatalyst was their reusability and recyclability. The results demonstrated that the $MnFe_2O_4$/GO/CS nanocomposite exhibited high recyclability, maintaining its dye removal capacity even after multiple rounds. This remarkable reusability characteristic is crucial for developing cost-effective and sustainable water treatment solutions. By allowing the photocatalyst to be regenerated and reused numerous times, the overall operational costs and environmental impact can be significantly reduced. Separation of the used $MnFe_2O_4$/GO/CS nanocomposite from the treated aqueous solution achieved by utilizing the magnetic properties of the nanocomposites via magnet, allowing for easy recovery and reuse after the photocatalytic treatment process. Following the separation, the recovered nanocomposite washed with water and ethanol to remove any residual dyes or contaminants that may have been adsorbed onto the surface during the treatment. This washing step would help regenerate the active sites on the nanocomposite, thereby preparing it for reuse in subsequent treatment cycles. The ability of the photocatalyst to retain their high adsorption performance after repeated use highlights their potential for practical applications in real-world wastewater treatment scenarios, particularly in the treatment of effluents from textile industries (Fig. 12).

The results of the current work were compared with those reported in the literature by other researchers (Table 2).

Dye degradation mechanism

The mechanism of dye degradation by the $MnFe_2O_4$/GO/CS nanocomposite can be explained as follows (Fig. 13). Under irradiation, the $MnFe_2O_4$ in the nanocomposite absorbs photons, generating electron-hole pairs. The excited electrons are transferred to the graphite oxide component, which is an efficient electron acceptor. The holes in $MnFe_2O_4$ react with water molecules to produce highly reactive hydroxyl radicals (•OH), which can oxidize the dye molecules. The electrons in GO can also react with dissolved oxygen to produce superoxide

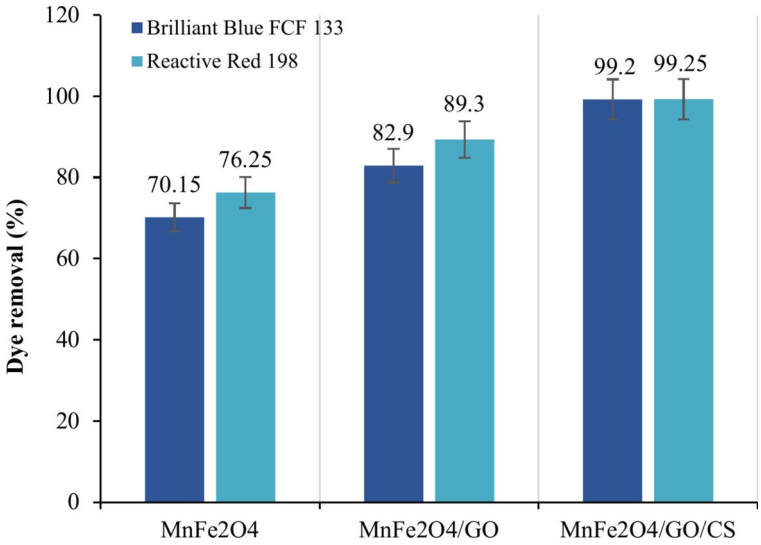

Fig. 10. Dye removal (%) under sunlight irradiation.

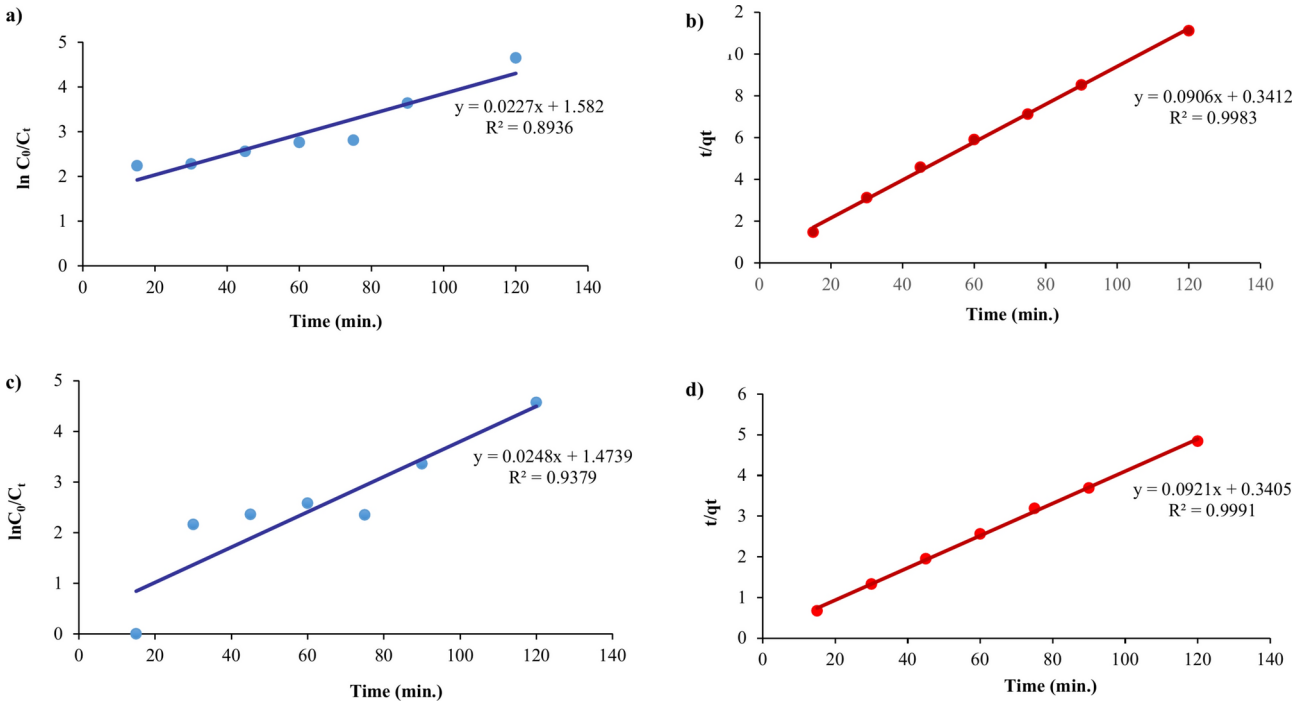

Fig. 11. Kinetics studies (**a**,**c**) Pseudo-first order and (**b**,**c**) Pseudo-second order using $MnFe_2O_4$/GO/CS on Reactive Red 198 (**a**,**b**) and Brilliant Blue FCF 133 (**c**,**d**) dyes.

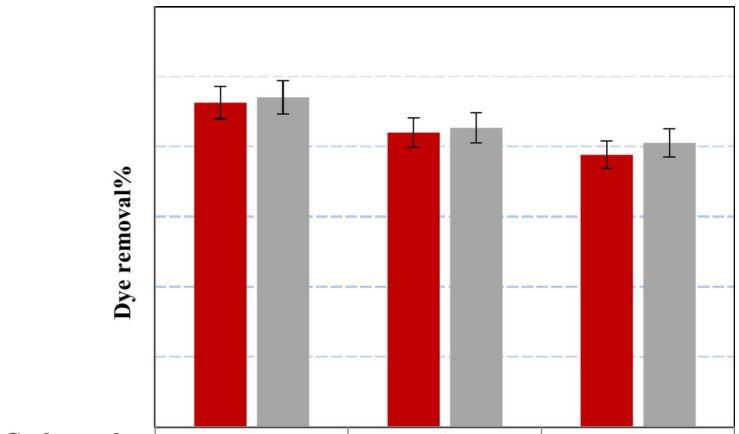

Cycle number	1	2	3
Blue 133	92.53	83.96	77.66
Red 198	94.01	85.35	81

Fig. 12. Dye removal (%) using $MnFe_2O_4$/GO/CS after three cycles.

radicals ($^{\bullet}O_2^-$), further contributing to the oxidative degradation of the dyes. The chitosan component provides additional adsorption sites, enhancing the capture and concentration of dye molecules on the nanocomposite surface, facilitating their interaction with the reactive species. The combined effects of the photocatalytic activity of $MnFe_2O_4$, the electron-accepting properties of GO, and the adsorption capacity of CS result in the efficient degradation of the Reactive Red 198 and Brilliant Blue FCF 133 dyes. These findings highlight the potential of the developed $MnFe_2O_4$/GO/CS nanocomposite as a versatile and effective photocatalyst for the treatment of textile wastewater containing a variety of dye pollutants.

Evaluation of dye removal on textile wastewater treatment

Textile wastewater is often heavily contaminated with dyes and other pollutants, posing a significant challenge for conventional treatment methods[31,32,34]. The reusability feature, combined with the outstanding photocatalytic performance demonstrated in the previous sections, underscores the versatility and applicability of these

Photocatalyst	Target dye	Dye removal (%)	Ref
$MnFe_2O_4$	Methylene blue	84	35
$MnFe_2O_4$/reduced graphene oxide	Methylene blue	97	35
$MnFe_2O_4$/coal fly ash	Methylene blue	99.9	36
$MnFe_2O_4$/multi wall carbon nanotube	Methylene blue	98	37
$MnFe_2O_4$/chitosan	Methyl orange	99.5	38
$MnFe_2O_4$/reduced graphene oxide/chitosan	Methylene blue	83.9	19
$MnFe_2O_4$/GO/CS	Reactive red 198	99.6	Current work
$MnFe_2O_4$/GO/CS	Brilliant blue FCF 133	99.9	Current work

Table 2. Comparison of dye photodegradation for different photocatalysts based on $MnFe_2O_4$.

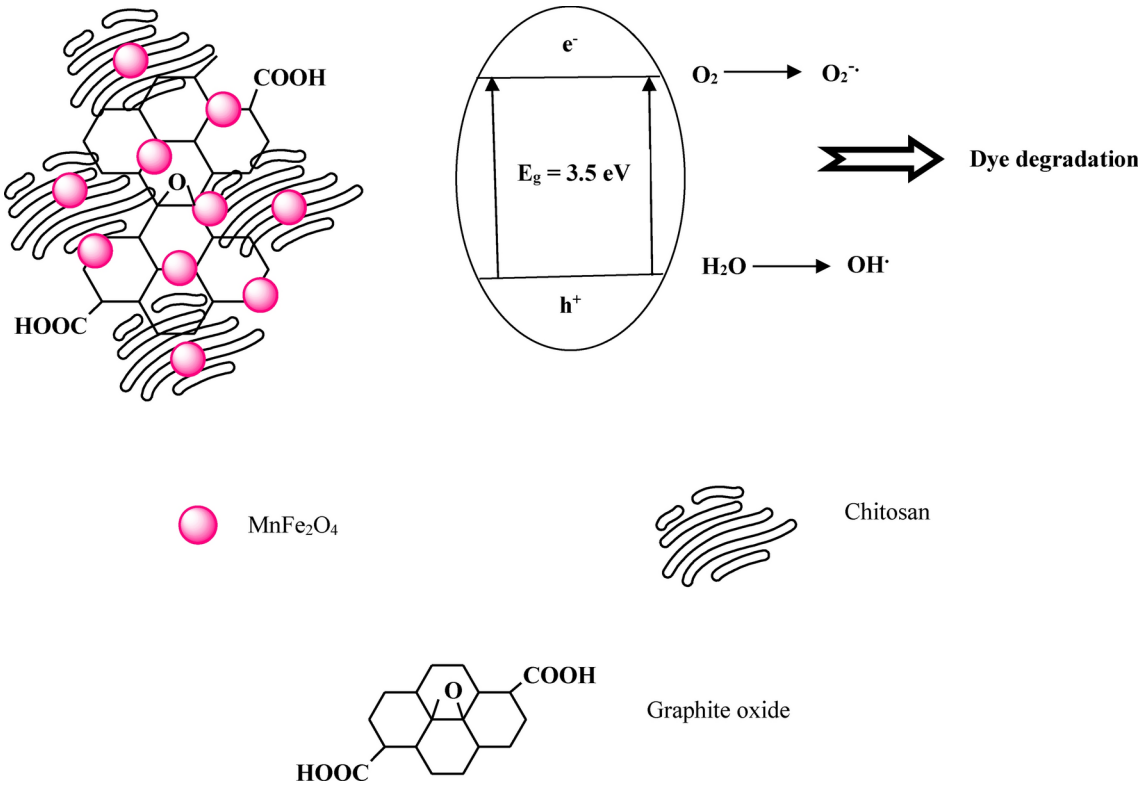

Fig. 13. Illustration of the proposed mechanism in photodegradation.

nanomaterials for comprehensive wastewater treatment in textile and other industrial sectors. To assess the performance of the $MnFe_2O_4$, $MnFe_2O_4$/GO, and $MnFe_2O_4$/GO/CS in real-world applications, the experiments were conducted using actual textile wastewater. First, the textile wastewater was passed through a 0.45 mm mesh filter paper to remove any suspended particles. This pre-treated wastewater sample was then subjected to the dye removal reaction under the optimal conditions previously determined. After the photocatalytic treatment, the initially colored textile wastewater became colorless, indicating the effective removal of the dye pollutants. To quantify the dye removal efficiency, we prepared a standard solution by mixing the Reactive Red 198 dye with the treated textile wastewater. Five volumetric flasks (25 mL) were filled with the colorless treated wastewater (20 mL), and different volumes (0, 1, 2, 4, and 5 mL) of the 100 mg/L standard dye solution were added to each flask. The flasks were then topped to the mark with distilled water and thoroughly mixed. The absorbance of the prepared samples was measured using a spectrophotometer. A calibration curve was constructed by plotting the absorbance values against known dye concentrations. The linear regression equation ($y = mx + b$) was derived using Microsoft Excel. To determine the concentration of dye remaining in the treated textile wastewater sample, we used the calibration curve equation, setting the absorbance (y) to 0 and solving for the concentration (x) of the textile wastewater sample. The results showed that the removal efficiency using $MnFe_2O_4$, $MnFe_2O_4$/GO, and $MnFe_2O_4$/GO/CS for the studied textile wastewater was 54.2, 76.21 and 96%, respectively. This high dye removal efficiency demonstrates the excellent performance of the $MnFe_2O_4$/GO/CS in treating real-world textile wastewater, which is a critical step toward their practical implementation in industrial wastewater treatment applications.

Evaluation of BOD and COD factors

To further assess the effectiveness of the $MnFe_2O_4$/GO/CS photocatalyst in treating textile wastewater, our group measured the levels of biochemical oxygen demand (BOD) and chemical oxygen demand (COD) before and after the photocatalytic treatment. The measurements were conducted by the Mahamax Company, a specialized laboratory. Before the photocatalyst treatment, the textile wastewater exhibited high levels of BOD and COD. The BOD and COD were measured at 889 and 1227 mg/L, respectively. However, after the photocatalytic treatment using the $MnFe_2O_4$/GO/CS nanocomposite, our group observed a significant reduction in both BOD and COD levels. The BOD was reduced from 889 to 0.86 mg/L, while the COD decreased from 1227 to 74 mg/L. These substantial reductions in BOD and COD levels demonstrate the remarkable ability of the $MnFe_2O_4$/GO/CS photocatalyst to effectively remove organic pollutants and improve the overall quality of the treated textile wastewater. The lowered BOD and COD values indicate a decreased demand for oxygen in the water, which is crucial for the prevention of oxygen depletion and the preservation of aquatic ecosystems. The successful treatment of textile wastewater, as evidenced by the significant reductions in BOD and COD, further highlights the potential of the $MnFe_2O_4$/GO/CS nanocomposite for practical applications in industrial wastewater treatment processes.

Conclusion

This study successfully demonstrated the hydrothermal synthesis and application of $MnFe_2O_4$-based nanocomposites for efficient dye removal from aqueous solutions and textile wastewater. The research focused on developing $MnFe_2O_4$, $MnFe_2O_4$/GO, and $MnFe_2O_4$/GO/CS nanocomposites, with extensive characterization to understand their structural, optical, and surface properties. XRD analysis confirmed the cubic spinel structure of $MnFe_2O_4$ with characteristic peaks, while SEM imaging revealed polyhedral $MnFe_2O_4$ particles deposited on a wrinkled graphite oxide matrix. The $MnFe_2O_4$/GO/CS nanocomposite exhibited a high specific surface area of 442.57 m^2/g with a pore diameter of 2.36 nm, as determined by BET analysis. DRS analysis indicated varying band gap energies for the nanocomposites, ranging from 3.0 to 3.5 eV. Regarding dye removal performance, the $MnFe_2O_4$/GO/CS nanocomposite demonstrated superior capabilities under various conditions. It achieved 99.9 and 99.5% removal efficiency of Reactive Red 198 and Brilliant Blue FCF 133, respectively. Kinetic studies revealed that the photocatalytic dye removal process followed pseudo-second-order kinetics, with an R^2 value of 0.99, providing insights into the photodegradation mechanism. The practical applicability of the nanocomposite was further demonstrated through its performance in treating real textile wastewater, where it achieved a 96% dye removal rate. Moreover, significant reductions in BOD (from 889 to 0.86 mg/L) and COD (from 1227 to 74 mg/L) levels were observed after treatment, indicating substantial improvement in water quality. The $MnFe_2O_4$/GO/CS nanocomposite also exhibited excellent reusability, maintaining high dye removal capacity over multiple cycles. This feature, combined with its effectiveness under UV and sunlight, underscores its potential as a sustainable and versatile solution for water purification challenges.

Data availability

The datasets used and/or analyzed during the current study available from the corresponding author on reasonable request.

Received: 1 July 2024; Accepted: 24 December 2024
Published online: 05 January 2025

References

1. Ali, S. et al. A critical review on the treatment of dye-containing wastewater: Ecotoxicological and health concerns of textile dyes and possible remediation approaches for environmental safety. *Ecotoxicol. Environ. Saf.* **231**, 113160 (2022).
2. Almroth, B. C. et al. Assessing the effects of textile leachates in fish using multiple testing methods: from gene expression to behavior. *Ecotoxicol. Environ. Saf.* **207**, 111523 (2021).
3. Bhattacharya, S., Gupta, A. B., Gupta, A, Pandey A. Introduction to water remediation: importance and methods. *Water Remediat.* 3-8 (2018).
4. Holkar, C. R., Jadhav, A. J., Pinjari, D. V., Mahamuni, N. M. & Pandit, A. B. A critical review on textile wastewater treatments: possible approaches. *J. Environ. Manag.* **182**, 351–366 (2016).
5. Solayman, H. M. et al. Performance evaluation of dye wastewater treatment technologies: A review. *J. Environ. Chem. Eng.* **11** (3), 109610 (2023).
6. Al-Tohamy, R. et al. A critical review on the treatment of dye-containing wastewater: Ecotoxicological and health concerns of textile dyes and possible remediation approaches for environmental safety. *Ecotoxicol. Environ. Saf.* **231**, 113160 (2022).
7. Samsami, S., Mohamadizaniani, M., Sarrafzadeh, M. H., Rene, E. R. & Firoozbahr, M. Recent advances in the treatment of dye-containing wastewater from textile industries: overview and perspectives. *Process Saf. Environ. Prot.* **143**, 138–163 (2020).
8. Kishor, R. et al. Ecotoxicological and health concerns of persistent coloring pollutants of textile industry wastewater and treatment approaches for environmental safety. *J. Environ. Chem. Eng.* **9**, 105012 (2021).
9. Katheresan, V., Kansedo, J. & Lau, S. Y. Efficiency of various recent wastewater dye removal methods: a review. *J. Environ. Chem. Eng.* **6** (4), 4676–4697 (2018).
10. Akhlaghi, N. & Najafpour-Darzi, G. Manganese ferrite ($MnFe_2O_4$) Nanoparticles: From synthesis to application—A review. *J. Ind. Eng. Chem.* **103**, 292–304 (2021).
11. Sharifi, S., Rahimi, K. & Yazdani, A. Highly improved supercapacitance properties of $MnFe_2O_4$ nanoparticles by MoS_2 nanosheets. *Sci. Rep.* **11**, 8378 (2021).
12. Simon, C. et al. Magnetic properties and structural analysis on spinel $MnFe_2O_4$ nanoparticles prepared *via* non-aqueous microwave synthesis. *ZAAC* **647** (22), 2061–2072 (2021).
13. Mounkachi, O. et al. Origin of the magnetic properties of MnFe2O4 spinel ferrite: Ab initio and monte carlo simulation. *J. Magn. Magn. Mater.* **533**, 168016 (2021).
14. Manohar, A., Krishnamoorthi, C., Pavithra, C. & Thota, N. Magnetic hyperthermia and photocatalytic properties of $MnFe_2O_4$ nanoparticles synthesized by solvothermal reflux method. *J. Supercond. Nov. Magn.* **34**, 251–259 (2021).

15. Desai, H. B., Hathiya, L. J., Joshi, H. H. & Tanna, A. R. Synthesis and characterization of photocatalytic $MnFe_2O_4$ nanoparticles. *Mater. Today Proc.* **21** (4), 1905–1910 (2020).
16. Palanivel, B., Shkir, M., Alshahrani, T. & Mani, A. Novel $NiFe_2O_4$ deposited S-doped g-C_3N_4 nanorod: Visible-light-driven heterojunction for photo-Fenton like tetracycline degradation. *Diam. Relat. Mater.* **112**, 108148 (2021).
17. Nawaz, A., Khan, A., Ali, N., Ali, N. & Bilal, M. Fabrication and characterization of new ternary ferrites-chitosan nanocomposite for solar-light driven photocatalytic degradation of a model textile dye. *Environ. Technol. Innov.* **20**, 101079 (2020).
18. Mishra, P., Behera, A., Kandi, D. & Parida, K. Facile construction of a novel $NiFe_2O_4$@P-doped g-C_3N_4 nanocomposite with enhanced visible-light-driven photocatalytic activity. *Nanoscale Adv.* **1**, 1864–1879 (2019).
19. Zhan, Y., Meng, Y., Xie, Z. & Wei, Z. Synthesis of chitosan/$MnFe_2O_4$@reduced graphene oxide aerogel with radial passageway and its application in removing methylene blue from water. *Funct. Mater. Lett.* **15** (2), 2251019 (2022).
20. Zourou, A. et al. Graphene oxide-$MnFe_2O_4$ nanohybrid material as an adsorbent of congo red dye. *J. Phys. Chem. Solids* **181**, 111490 (2023).
21. Alaqarbeh, M., Khalili, F., Bouachrine, M. & Alwarthan, A. Synthesis, characterization and investigation of cross-linked chitosan/($MnFe_2O_4$) nanocomposite adsorption potential to extract U(VI) and Th(IV). *Catalysts* **13**, 47 (2023).
22. Mahdavinasab, M., Hamzehlouеian, M. & Sarrafi, Y. Preparation and application of magnetic chitosan/graphene oxide composite supported copper as a recyclable heterogeneous nanocatalyst in the synthesis of triazoles. *Int. J. Biol. Macromol.* **138**, 764–772 (2019).
23. Mukherjee, A., Dhak, P. & Dhak, D. The solvothermal synthesis of a 3D rod-like Fe-Al bimetallic metal–organic-framework for efficient fluoride adsorption and photodegradation of water-soluble carcinogenic dyes. *Environ. Sci. Adv.* **1**, 121–137 (2022).
24. Mukherjee, A., Adak, M. K., Dhak, P. & Dhak, D. A simple chemical method for the synthesis of Cu^{2+} engrafted $MgAl_2O_4$ nanoparticles: Efficient fluoride adsorbents, photocatalyst and latent fingerprint detection. *J. Environ. Sci.* **88**, 301–315 (2020).
25. Mukherjee, A., Dhak, P., Mandal, D. & Dhak, D. Solvothermal synthesis of 3D rod-shaped Ti/Al/Cr nano-oxide for photodegradation of wastewater micropollutants under sunlight: a green way to achieve SDG: 6. *Environ. Sci. Pollut. Res.* https://doi.org/10.1007/s11356-023-30112-8 (2023).
26. Mukherjee, A., Dhak, P., Hazra, V., Goswami, N. & Dhak, D. Synthesis of mesoporous Fe/Al/La trimetallic oxide for photodegradation of various water-soluble dyes: Kinetic, mechanistic, and pH studies. *Environ. Res.* **217**, 114862 (2023).
27. Fazeleh, K., Shokrollahzadeh, S., Bide, Y., Sheshmani, S. & Shahvelayati, A. S. High- flux sodium alginate sulfate draw solution for water recovery from saline waters and wastewaters via forward osmosis. *Chem. Eng. J.* **417**, 129250 (2021).
28. Hosseinzadeh, S., Eslami Moghadam, M., Sheshmani, S. & Shahvelayati, A. S. Some new anticancer platinum complexes of dithiocarbamate derivatives against human colorectal and pancreatic cell lines. *J. Biomol. Struct. Dyn.* **38**, 2215–2228 (2020).
29. Soleimannejad, J. et al. Different complexation behavior of Fe(III), Co(II) and Ni(II) with pyridine-2,6-dicarboxylic Acid and 4,4′-bipyridine adduct: Syntheses, crystal structures and solution studies. *J. Iran. Chem. Soc.* **8**, 247–264 (2011).
30. Aghabozorg, H., Soleimannejad, J., Sharif, M., Sheshmani, S. & Moghimi, A. Crystal structure of a proton-transfer compound between 2,6-pyridinedicarboxylic acid and N, N′-diethyl-2-amino-6-methyl-4-pyrimidinol. *Anal. Sci. X-ray Struct. Anal.* **21**, x73–x74 (2005).
31. Qamar, M. A. et al. Progress in the development of phyto-based materials for adsorption of dyes from wastewater: A review. *Mater. Today Commun.* **38**, 108385 (2024).
32. Le, T. T. H., Ngo, T. T., Han, T. P. N. & Chu, T. T. Post-adsorption properties and thermodynamic adsorption parameters of various graphene oxide-based materials. *Chem. Select* **9**, e202401493 (2024).
33. Thakur, A., Kumar, A. & Singh, A. Adsorptive removal of heavy metals, dyes, and pharmaceuticals: Carbon-based nanomaterials in focus. *Carbon* **217** (25), 118621 (2024).
34. Mukherjee, A., Goswami, N. & Dhak, D. Photocatalytic remediation of industrial dye waste streams using biochar and metal-biochar hybrids: A critical review. *Chem. Afr.* **6**, 609–628 (2023).
35. Mandal, B., Panda, J., Paul, P. K., Sarkar, R. & Tudu, B. $MnFe_2O_4$ decorated reduced graphene oxide heterostructures: Nanophotocatalyst for methylene blue dye degradation. *Vacuum* **173**, 109150 (2020).
36. Mushtaq, F. et al. $MnFe_2O_4$/coal fy ash nanocomposite: a novel sunlight-active magnetic photocatalyst for dye degradation. *Int. J. Environ. Sci. Technol.* **17**, 4233–4248 (2020).
37. Hazarika, M. et al. Investigating the impact of structural defects in MWCNT/$MnFe_2O_4$ nanocomposite for efficient photodegradation of cationic dye. *Phys. Rev. B Condens.* **675**, 415598 (2024).
38. Wang, Z., Li, Y., Xie, X. & Wang, Z. Bifunctional $MnFe_2O_4$/chitosan modified biochar composite for enhanced methyl orange removal based on adsorption and photo-fenton process. *Coll. Surf. A: Physicochem. Eng. Asp.* **613**, 126104 (2021).

Author contributions

Nazila Mohammad Hosseini: Development and design of methodology; Investigation. Shabnam Sheshmani: Supervision, Conceptualization, Development and design of methodology; Investigation; Writing-Reviewing Ashraf S. Shahvelayati: Validation.

Declarations

Competing interests

The authors declare no competing interests.

Additional information

Correspondence and requests for materials should be addressed to S.S.

Reprints and permissions information is available at www.nature.com/reprints.

Publisher's note Springer Nature remains neutral with regard to jurisdictional claims in published maps and institutional affiliations.